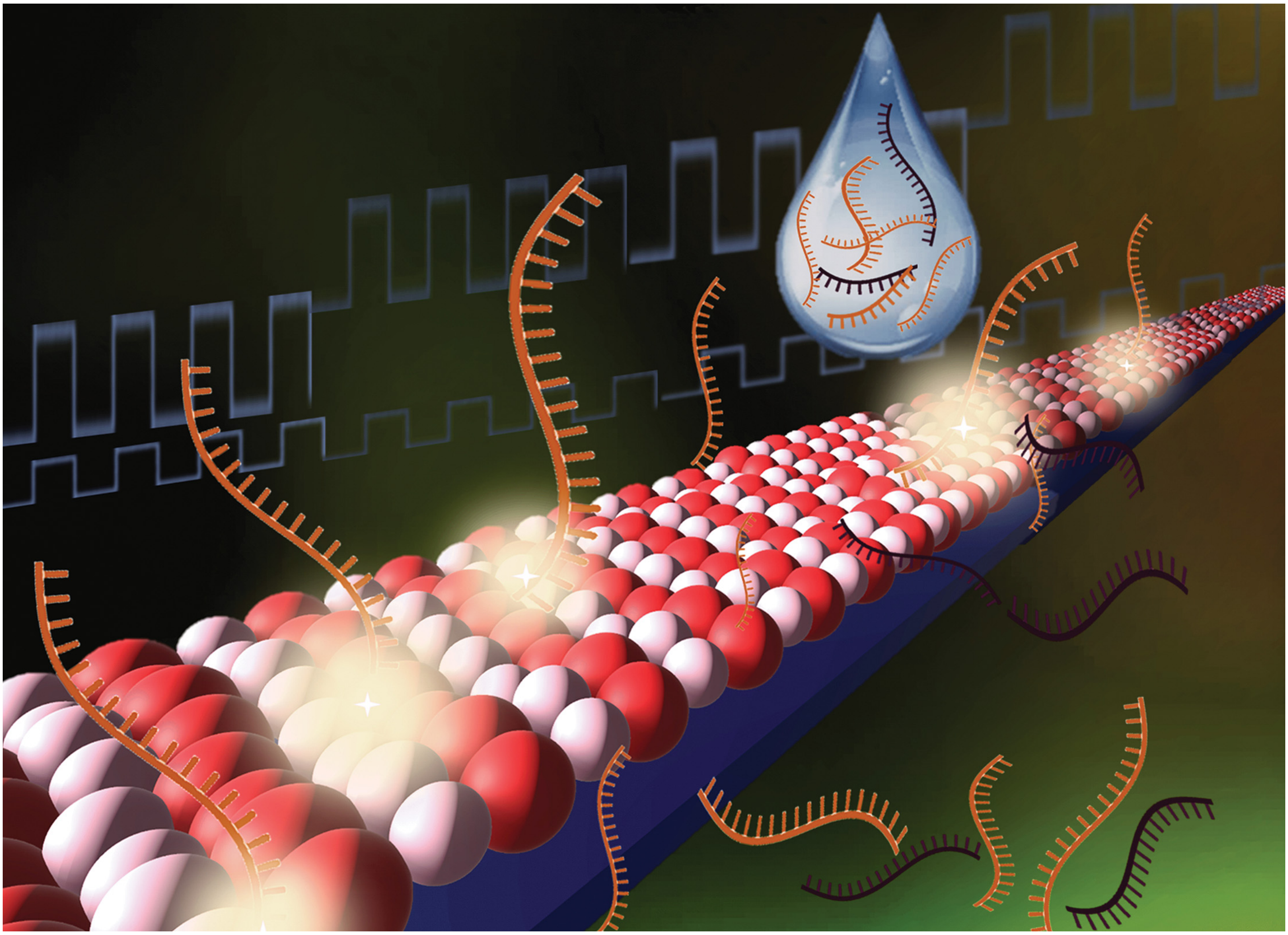

Showcasing collaborative research work from the Group of Prof. Arindam Mondal, Chandra Sekhar Tiwary at Indian Institute of Technology Kharagpur and Prabal K Maiti at Indian Institute of Science Bangalore, India

Utilization of DNA and 2D metal oxide interaction for an optical biosensor

The combined experimental and theoretical work establishes an understanding of the interaction between DNA and a two-dimensional (2D) metal oxide for developing a biosensor for detection of viral infections. The spectroscopy analysis demonstrates the chemical interaction between single-stranded DNA (ssDNA) and 2D metal oxide which is further explained with theoretical simulation. Our investigation opens the pathway to develop a cost-effective, diagnostic biosensor with high sensitivity.

As featured in:

See Arindam Mondal, Prabal K Maiti, Chandra Sekhar Tiwary *et al.*, *Phys. Chem. Chem. Phys.*, 2023, **25**, 17143.

ROYAL SOCIETY OF CHEMISTRY

rsc.li/pccp

Registered charity number: 207890

PCCP Owner Societies

PCCP

PAPER

View Article Online
View Journal | View Issue

Check for updates

Cite this: *Phys. Chem. Chem. Phys.*, 2023, **25**, 17143

Utilization of DNA and 2D metal oxide interaction for an optical biosensor†

Partha Kumbhakar, ‡§[a] Indrani Das Jana,‡[b] Subhadip Basu, ‡[c] Sandip Mandal,[c] Saptarshi Banerjee,[b] Subhanita Roy,[b] Chinmayee Chowde Gowda, [d] Anyesha Chakraborty,[d] Ashim Pramanik,[ae] Pooja Lahiri,[f] Basudev Lahiri,[g] Amreesh Chandra,[h] Pathik Kumbhakar, [e] Arindam Mondal,*[b] Prabal K Maiti *[c] and Chandra Sekhar Tiwary *[a]

Received 28th March 2023,
Accepted 26th May 2023

DOI: 10.1039/d3cp01402a

rsc.li/pccp

The efficient monitoring and early detection of viruses may provide essential information about diseases. In this work, we have highlighted the interaction between DNA and a two-dimensional (2D) metal oxide for developing biosensors for further detection of viral infections. Spectroscopic measurements have been used to probe the efficient interactions between single-stranded DNA (ssDNA) and the 2D metal oxide and make them ideal candidates for detecting viral infections. We have also used fully atomistic molecular dynamics (MD) simulation to give a microscopic understanding of the experimentally observed ssDNA-metal oxide interaction. The adsorption of ssDNA on the inorganic surface was found to be driven by favourable enthalpy change, and 5′-guanine was identified as the interacting nucleotide base. Additionally, the *in silico* assessment of the conformational changes of the ssDNA chain during the adsorption process was also performed in a quantitative manner. Finally, we comment on the practical implications of these developments for sensing that could help design advanced systems for preventing virus-related pandemics.

1. Introduction

Functionalization of any inorganic-material surface for efficient biomolecule capturing symbolises a biosensor. Considering the ongoing SARS-CoV-2 pandemic, the generation of a cost effective, rapid and highly sensitive device for the early detection of the virus is of utmost importance these days. In this regard, researchers have come up with a number of quick detection strategies in the form of biosensors. A field effect transistor (FET)-based biosensor generated by coating graphene sheets of the FET with a specific antibody against SARS-CoV-2 spike protein can detect 2.42×10^{2} copies mL^{-1} of the virus from nasopharyngeal swab specimens of COVID-19 patients.[1] Recently, Mahari *et al.*, have developed a eCovSens device fabricated with a fluorine doped tin oxide (FTO) electrode along with AuNPs and nCOVID-19 antibody to specifically detect the nCOVID-19 spike antigen ranging from 1 fM to 1 μM concentrations within 10–30 s.[2] A surface plasmon resonance (SPR)-based biosensor coated with a peptide monolayer and functionalized with SARS CoV-2 nucleocapsid (NC) recombinant protein can detect SARS-CoV-2 NC antibodies in human serum samples in the nM range within 15 min of sample/sensor contact.[3] An engineered RNA biosensor PHAsed NASBA-translation optical method (PHANTOM) is capable of detecting as low as 100 copies of SARS-CoV-2 RNA in patient samples.[4] However, none of the biosensors discussed so far are based on the principle of nucleic acid hybridization to detect SARS CoV-2 RNA.

A number of nucleic acid-based biosensors have been reported to-date with wide scalability of detecting pathogen-associated nucleic acids for rapid, point-of-care (POC) diagnosis of infectious diseases.[5–8] These nucleic acid-based biosensors provide a highly sensitive and selective platform for detecting target nucleic acids

---

[a] *Department of Metallurgical and Materials Engineering, Indian Institute of Technology Kharagpur, Kharagpur 721302, India. E-mail: chandra.tiwary@metal.iitkgp.ac.in*
[b] *School of Bioscience, Indian Institute of Technology Kharagpur, Kharagpur 721302, India. E-mail: arin.cal@gmail.com*
[c] *Centre for Condensed Matter Theory, Department of Physics, Indian Institute of Science, Bangalore 560012, India. E-mail: maiti@iisc.ac.in*
[d] *School of Nano Science and Technology, Indian Institute of Technology Kharagpur, Kharagpur 721302, India*
[e] *Nanoscience Laboratory, Department of Physics, National Institute of Technology Durgapur, 713209, India*
[f] *School of Medical Science and Technology, Indian Institute of Technology Kharagpur, Kharagpur 721302, India*
[g] *Department of Electronics and Electrical Communication Engineering, Indian Institute of Technology Kharagpur, Kharagpur 721302, India*
[h] *Department of Physics, Indian Institute of Technology Kharagpur, Kharagpur 721302, India*

† Electronic supplementary information (ESI) available. See DOI: **https://doi.org/10.1039/d3cp01402a**

‡ Equal contribution.

§ Current address: Department of Physics and Electronics, CHRIST (Deemed to be University), Bangalore 560029, India.

(RNA/DNA) at material surfaces. The material surfaces are functionalized with complementary single-stranded oligonucleotides. A variety of DNA-decorated metal-based biosensors have been reported so far with a wide range of applications, including lateral-flow biosensors for POC nucleic acid tests, DNA microarrays, and silicon nanowire (Si NW)-based sensors for the detection of dengue virus serotype 2 (DENV 2) as well as influenza A virus (IAV) RNA. Similarly, a functionalized poly-crystalline Si NW field-effect transistor (FET)-based sensor for the detection of the highly pathogenic IAV virus (H5 and H7) strain has also been reported. Peptide nucleic acid (PNA)–DNA probes have been used for the detection of virus- and other pathogenic bacteria-mediated infections, further highlighting the applications of these DNA-based metal biosensors.[6,9–13] ssDNA immobilized on capacitive field effect sensors modified with a polyelectrolyte layer (PAH) can be effectively used to capture target cDNA molecules.[14] Cherstvy *et al.* calculated the electrostatic interactions possibly taking place upon DNA hybridization in dense DNA arrays immobilized on a layer of Au nanoparticles deposited on the surface of a field effect-based DNA capacitive biosensor.[15] Recently, a 2D Au nano-island functionalised with cDNA, in combination with the plasmonic photothermal effect and localized surface plasmon resonance (LSPR) sensing technique, was used for detecting SARS CoV-2 in clinical COVID-19 samples with a limit of up to 0.22 pM concentration.[16]

While covalent modification of DNA has been a popular method to achieve highly stable and directional linkage in most DNA-based biosensors, physio-sorption is also considered a cost-effective and straightforward alternative. In recent times, DNA-based biosensors have been improvised extensively to expand their range of applications in molecular diagnostics. In this regard, interfacing two-dimensional (2D) metal oxides with DNA has yielded numerous new hybrids with enhanced efficiency for biosensing.[17–21] 2D oxides like graphene oxide (GO), MXenes, MoS_2 and WS_2 exhibit interesting surface properties like high surface charge, good conductivity and excellent ease of functionalization. They can easily adsorb any charged molecules or metal ions and are usually coated with inorganic materials such as nitrogen, sulphur, oxygen, *etc.*, which enhances the charge or electron transfer between nanomaterials and biomolecules.[22–26] Together, these properties make 2D materials excellent candidates for various biosensing devices. Furthermore, these materials are eligible to passively adsorb biomolecules and participate in active chemical interaction with the same. The functionalized graphene can easily detect several biomolecules like DNA, enzymes, proteins, antigens, and antibodies owing to its own oxide components like the epoxide, hydroxyl, and carboxyl groups formed on its edge on the surface.[27] It has been reported earlier that GO mainly adsorbs DNA molecules by π–π stacking and hydrogen bonding with the same.[28] On the contrary, MoS_2 and WS_2 mostly rely on van der Waals interactions to initiate their DNA attachment.[29–32] Recently, amino-modified DNA attached to polyacrylic acid-modified Ti_3C_2 MXene has rendered a biosensor that is utilized to detect cancer biomarkers.[33] Among other 2D metal-oxides, Mn_3O_4 exhibiting catalytic properties has been reported recently.[34]

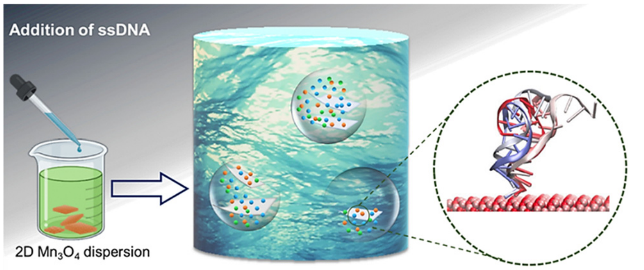

Fig. 1 (a) Schematic illustration showing the interaction of single stranded DNA with 2D Mn_3O_4.

Encouraged by the extraordinary properties of random physio-sorption of DNA by various 2D materials, we intended to design an ssDNA bound-2D Mn_3O_4 as an optical biosensor. However, the DNA binding properties of 2D materials and the fundamental mechanism behind the same are yet to be investigated. Here we study the surface chemistry of Mn_3O_4 and the DNA adsorption properties of 2D Mn_3O_4 to explore the possibilities of its functionalization as a biosensor (Fig. 1). In this context, we systematically studied the adsorption of DNA oligonucleotides on 2D Mn_3O_4 by UV visible absorption and photoluminescence (PL) spectroscopic measurements. The functionalized Mn_3O_4 supports the immobilization of DNA probes in a biocompatible manner. The PL emission and FTIR data revealed the unique role of Mn^{2+}/Mn^{3+} and highlights its interaction with DNA adsorption. The atomistic calculations confirm the experimental observations. Finally, we utilized the ssDNA-immobilized 2D Mn_3O_4 for specific capturing of complementary RNA and fused it with reverse transcription loop-mediated isothermal amplification (RT-LAMP) for colorimetric endpoint detection, presenting the proof of concept for a novel, 2D Mn_3O_4-based biosensor for specific detection of nucleic acids. This technology could pave the way for the development of a rapid, cost effective and highly sensitive diagnostic biosensor that can be utilized in future to detect not only Covid 19 but also a plethora of infections caused by a wide variety of pathogens.

2. Materials and methods

2.1. Synthesis

The custom-designed DNA samples and primers used in this study were procured from Integrated DNA Technologies (IDT) (Table 1 and Tables S1–S3, ESI†) and stored at −20 °C. All the experiments were carried out at room temperature or 25 °C unless otherwise specified.

Hausmannite nanoparticles were synthesized by a co-precipitation method. 0.22 M of manganese chloride tetrahydrate ($MnCl_2{\cdot}4H_2O$) and 1.37 mM hexadecyl trimethyl-ammonium bromide (CTAB) were added under constant stirring. 0.44 M of sodium hydroxide (NaOH) solution was prepared separately, added dropwise to the first solution, and constantly stirred for 24 h. The final product was filtered and washed with DI water and then ethanol 3–4 times. The material was then dried in an oven at 80 °C overnight. The large-scale synthesis of 2D Mn_3O_4 was obtained by the liquid phase exfoliation (LPE) technique

Table 1 Sequences of DNA oligonucleotides used in this study

ID	DNA oligonucleotides	5′–3′ Sequences
01	ss DNA	GCAGCCGCTCCACCAAGCCAAAGTAGAACGCAGT
02	ss DNA-FAM_2	FAM-GATTAGTTCCTGGTCCCCAAAATTTCC

using a probe sonication method. To break the covalent bonds between layers, the surface energy of the solvent becomes crucial during exfoliation. With *iso*-propanol as a solvent, powdered hausmannite obtained by co-precipitation was exfoliated in this medium. The concentration of the sample to solvent ratio was of the order 1 : 500 mg mL^{-1}. The probe-sonicator frequency was at 30 KHz and exfoliation was done in pulses of 10 s each, for 2 hours. The sample suspension was extracted and dried at 40 °C to obtain the powdered sample.

The optical absorbance properties of pristine hausmannitene was characterized using a UV-vis spectrometer (HITACHI, U3010) from 200–800 nm. We then used transmission electron microscopy (TEM) to analyze the sample further. A TEM FEI-TECHNAI G220S-Twin was utilized to obtain high-resolution TEM micrographs. Atomic force microscopy (AFM) was performed using an Agilent Technologies Model No. 5500. The drop deposition technique was used for the sample deposition on a monocrystalline silicon substrate.

2D Mn_3O_4 particles stabilized by ssDNA were prepared by adding 500 nM of ssDNA (Table 1) to 200 μL of an aqueous Mn_3O_4 solution (0.3 mg mL^{-1}). The sample was incubated at room temperature (RT) with continuous stirring for 30 min, and centrifuged to remove any excess of unbound ssDNA from the supernatant. The pellet was then re-suspended in a similar volume of Milli-Q water. The absorbance spectra of the ssDNA bound to the 2D Mn_3O_4 nanoparticles were acquired by using a spectrophotometer (HITACHI, U3010). For the DNA adsorption capacity study, 2D Mn_3O_4 particles (0.3 mg mL^{-1}) were dispersed in water by sonication for 30 s followed by adding different concentrations of ssDNA ranging from 10 nM to 2 μM. The DNA adsorption capacity was measured by acquiring the spectral reading at 30 min by using a spectrophotometer (Epoch 2 microplate reader) within the 200–500 nm wavelength. Time kinetics for the DNA adsorption study was further performed wherein kinetic and spectral analyses were carried out at RT for different time intervals. The ssDNA (0.5 μM) adsorbed on aqueous 2D Mn_3O_4 (0.3 mg mL^{-1}) solution was drop cast on a UV sterilized glass slide and allowed to vacuum dry completely in a desiccator. The samples were then preceded for FTIR analysis. Furthermore, the sample was used for AFM analysis wherein a droplet of the same was spotted onto a silica substrate and vacuum dried completely. The image of the ssDNA fragment adsorbed on the 2D Mn_3O_4 particle was taken in the air using an Agilent Technologies Model No. 5500. For optical imaging, the 2D Mn_3O_4 were sonicated for 30 s in a bath sonicator at RT, and vortexed for 30 s prior to use. 10 μM of FAM-ssDNA (Table 1) was added to 200 μL of an aqueous solution of Mn_3O_4. The resulting mixture was then stirred at RT for 30 min and the sample was drop cast on a clean UV sterilized glass slide and proceeded for optical imaging using a fluorescence microscope (Leica Microsystems). The images were taken under 10× and 45× resolution.

2.2. *In vitro* transcription of SARS-CoV-2 sub genomic RNA

RNA (283 nt) used in this study (Table S3, ESI†) was *in vitro* transcribed from a gene block sequence purchased from Invitrogen (USA) and cloned in pUC 19 vector (NEB). A small double-stranded DNA containing region from 15 058 to 15 337 nucleotide of SARS-CoV-2-Wuhan-Hu-1 genome (accession number: NC_045512) preceded by T7 RNA polymerase promoter was synthesized from Invitrogen. PCR amplification of the DNA was performed using Phusion™ High-Fidelity DNA Polymerase (Thermo ScientificTM F530S) using primers listed in Table 2 (ESI†). 1 μg of the PCR amplified DNA was used as a template for *in vitro* transcription by using T7 RNA polymerase (Thermo ScientificTMEP0111) following the manufacturer's protocol. After transcription, the reaction was treated with DNase(Qiagen) for 1 hour at 37 °C. RNA was purified by TRIzol^{TM} reagent (Invitrogen^{TM}) and stored at −80 °C.

2.3. ssDNA–RNA hybridization

Capturing complementary RNA by the ssDNA bound Mn_3O_4 nanosheets was carried out by the hybridization process wherein 60 μL of the Mn_3O_4 particles (300 μg mL^{-1}) were added on to the UV sterilized glass slide coated with PVDF agent, followed by drying in a desiccator overnight. Any unbound DNA was removed henceforth by washing with ice-cold water. Next, 30 μL of ssDNA, Covid-19C-LOOP_F (50 μM) was dropcast on the chip and allowed to dry completely. Complementary 283 nt long SARS CoV-2 RNA (100 μg μL^{-1}) was preheated at 65 °C for 5 min followed by direct addition on to a ssDNA-Mn_3O_4 chip for 20 min at RT. Any unbound RNA was removed by rinsing with ice cold water, thrice. The RNA was then eluted with 20 μL of preheated water at 65 °C and added to RT-LAMP 2X RT mix from AURA (MPL-1). A 10 μL reaction was established by using the RNA, LAMP 2X RT mix and the primer mix comprising of six different LAMP primers (FIP, BIP, LF, LB, F3, and B3) (Table S2, ESI†) designed specifically against the RdRp gene of SARS CoV-2. The LAMP reaction procedure comprises heating the reaction mix at 60 °C for 40 minutes followed by inactivation at 95 °C for 5 minutes. The presence of RNA was detected by a significant change in the colour of the reaction mixture from violet to blue.

2.4. MD simulations

The structure of the Mn_3O_4 unit cell, with lattice parameters, $a = 5.870$ Å, $b = 6.348$ Å, $c = 5.873$ Å, $\alpha = 117.493°$, $\beta = 90.0°$, and $\gamma = 117.653°$, was obtained from the Materials Project database (ID: mp-18759).[35] The Lennard-Jones (LJ) force field parameters for Mn and O atoms were taken from the literature.[36,37] Restrained electrostatic potential atomic partial (RESP) charges on Mn and O in Mn_3O_4 were calculated using GAUSSIAN 09 (by means of B3LYP/6-31G(d) level of theory) and ANTECHAMBER module.[38,39] The estimated values of RESP charges on Mn and O, in Mn_3O_4 were found to be 0.3394 and −0.2546, respectively. A ssDNA segment with the nucleotide sequence 5′-GTAGAACGCAGT-3′ was built using the nucleic acid builder (NAB) module.[40] AMBER 14SB-OL15 force field parameters were used to describe the interactions involving DNA.[41] The total charge on the DNA segment was −11.0 e.

A Mn_3O_4 slab with dimensions of 4.76 × 5.13 × 1.6 nm^3 was built and placed inside a simulation box of 4.76 × 5.13 × 6.0 nm^3. In harmony with the experimental findings, the ssDNA segment was placed on the (001) facet of the slab in such a manner that the initial distance between the center of mass (COM) of the ssDNA and the surface was 1.3 nm. The combined system of the ssDNA and Mn_3O_4 slab was solvated with the TIP3P water model. Counter ions were added to neutralize the system. A total of 3829 water molecules with 11 Na^+ ions were added and the system contains a total of 15 311 atoms. Periodic boundary conditions were applied in all three dimensions. The system was first energy minimized for 100 000 steps using the steepest descent algorithm to remove close contacts between atoms. The minimized system was equilibrated at 300 K for 1 ns, using a modified Berendsen thermostat[42] with a coupling constant of 0.1 ps. A second phase of equilibration was carried out for 2 ns at a 1 bar pressure, using the Berendsen barostat[43] with a coupling constant of 20.0 ps. The equilibrated system was then subjected to a production *NPT* run for 300 ns.

A Parrinello–Rahman barostat with a coupling constant of 20.0 ps was employed for pressure coupling, during the production run.[44] The integration time step was 1 fs during both equilibration and production runs, and the trajectory was recorded every 2.5 ps interval for subsequent analysis. The Mn_3O_4 slab was kept restrained throughout the simulation. Position restraints were applied on the ssDNA during the equilibration phase only. The average cross-sectional area of the simulation box remained stable during the production run (26.71 ± 0.02 nm^2; also see Fig. S9 of ESI†). The LINCS algorithm was used to constraint all bonds involving hydrogen atoms.[45] The particle mesh Ewald (PME) summation technique was used to calculate the long-range coulombic interaction.[46] A cut-off distance of 1.0 nm was used for computing the short-range L-J interactions and short range part of the coulomb interactions. To understand the effect of the substrate, the ssDNA segment was also simulated in the absence of the Mn_3O_4 slab, following the same protocols as described above. All the simulations were performed using the GROMACS 5.1.5 package and VMD 1.9.3 software was used for visualization.[47,48] All analysis was performed using GROMACS modules or in-house TCL scripts. Calculation of binding energy was carried out using the MM-GBSA method,[49] incorporated in gmx_MMPBSA,[50] a tool based on the MMPBSA.py module of AMBER20.[51] The trajectory of the last 100 ns simulation was used for MM-GBSA calculation. Change in entropy due to DNA binding was calculated using a two-phase thermodynamic (2PT) model.[52,53] 2PT entropy is calculated by decomposing the density of states (DoS) of the system into a solid like and a gas like component. Anharmonicity is treated using the gas like component. The DoS function can be calculated from the Fourier transform of the velocity autocorrelation function, which provides information on the normal mode distribution of the system, with the zero frequency intensity in DoS corresponding to the diffusivity of the system.[52,53] The 2PT method has been successfully used to compute the entropy changes of DNA, while binding to the dendrimer, CNT and graphene.[54–57]

3. Results and discussion

The present study reveals the interaction between ssDNA and a 2D metal oxide. The attachment of ssDNA on the 2D Mn_3O_4 surface is confirmed by AFM, UV-vis absorption spectroscopy, PL emission spectroscopy, and FTIR data. The synthesized 2D Mn_3O_4 is characterized by AFM and TEM analyses (Fig. 2a and b). The successful synthesis of crystalline 2D Mn_3O_4 is confirmed by AFM measurement The line profile showing the thickness of each sheet is ∼3–4 nm. Fig. 2b shows the TEM image of the sample. The inset of Fig. 2b shows the high-resolution TEM image of Mn_3O_4 with well-defined lattice spacing. The crystal lattice fringes with *d*-spacing of ∼0.46 nm correspond to the (101) plane. The EDX result confirms the presence of Mn and O (Fig. S1, ESI†) along with Cu and C. The weight percentage of Mn and O is ∼47.27% and 38.56%, respectively. The presence of Cu and C originated from the holey carbon-coated copper grid. AFM study has been carried out to check the attachment of DNA on the 2D Mn_3O_4 surface. Fig. 2a displays the AFM image of the 34 nulclotide (nt) long DNA on 2D Mn_3O_4 after its binding. The DNA appears as a long filament with a uniform thickness-like structure that remains anchored at one of its ends on the surface of the 2D metal oxide. UV-vis absorption spectroscopy is a useful technique to investigate the binding and interaction characteristics of any molecule with DNA. Fig. 2d shows the absorption spectra of DNA, Mn_3O_4 and their mixture. The time-dependent changes during the attachment of DNA and Mn_3O_4 are also determined by using UV-vis absorption spectroscopic measurement. It shows a sharp band at ∼260 nm due to the purine and pyrimidine bases, whereas Mn_3O_4 shows a broad absorption band at ∼360 nm in the UV-vis region and it is attributed to the $O^{2-} \rightarrow Mn^{2+}$ and $O^{2-} \rightarrow Mn^{3+}$ charge transfer transitions.[34,58] In Fig. 2e, we present time-dependent UV-vis absorption spectra of DNA_Mn_3O_4. It is found that after attachment of DNA with Mn_3O_4, the absorption spectrum changes noticeably.

The absorption intensity at ∼360 nm is found to decrease continuously with time. The change of peak intensity as a function of interaction time is displayed in Fig. 2f. The well-known interaction modes are intercalation, minor/major groove binding, and electrostatic interaction with the phosphate backbone.[30,59,60] Thus, the UV-vis spectra indicate that the adsorption of DNA onto the Mn_3O_4 surface enhances with the increase in time. Photoluminescence (PL) emission spectroscopy is a non-destructive technique to identify the surface properties of the materials. Here, we have measured the PL emission spectra of Mn_3O_4, DNA and the mixture of Mn_3O_4 and DNA at different time intervals (Fig. 2g). Previous studies have shown the binding of FAM labelled DNA with various materials.[52] However, in our case, we have used non-fluorescent DNA and carefully intended to investigate the changes in PL emission properties of Mn_3O_4 after binding/interaction with DNA. From Fig. 2g it can be observed that there is a prominent luminescence

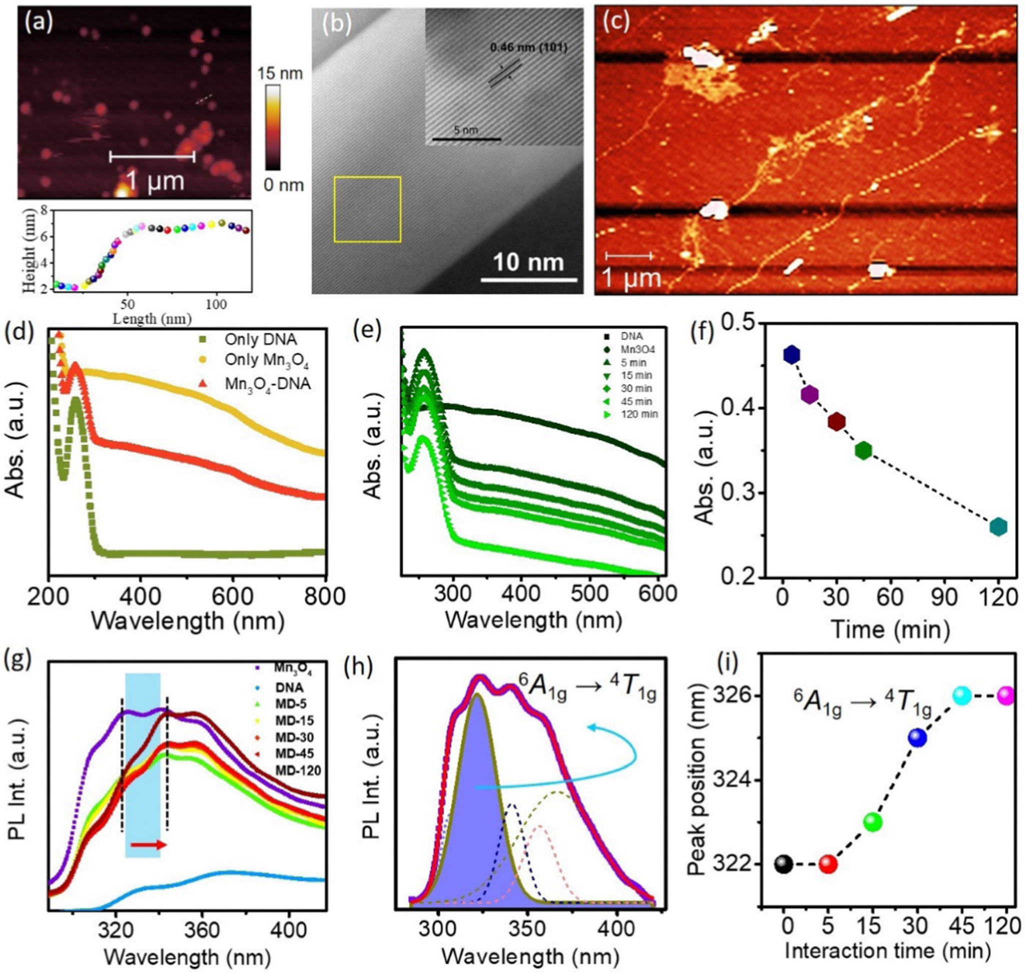

Fig. 2 (a) AFM image of the of Mn_3O_4. Lower inset shows the line scan of the sheets. (b) TEM image of Mn_3O_4. High resolution TEM image with the crystalline plane (inset). (c) AFM image of the sample after binding with ssDNA. (d) Absorption spectra of Mn_3O_4, DNA and their mixture. (e) Absorption spectra of the mixture as a function of interaction time. (f) Changes in the absorption intensities of DNA and Mn_3O_4 with time. (g) PL emission spectra Mn_3O_4 and DNA mixture as a function of interaction time. (h) De-convoluted PL emission spectra of 2D Mn_3O_4. (i) Peak position changes with interaction time.

for 2D Mn_3O_4. The emission peak at ~320 nm is attributed to $^6A_{1g} \rightarrow {}^4T_{1g}$ transition of Mn ions.[61–63] After the addition of DNA, the PL emission intensity is found to be quenched with prominent peak shifting (Fig. 2g), further confirming the adsorption of the DNA on the 2D Mn_3O_4. To get more information, we have fitted the PL emission spectra using the Gaussian multiple peak fitting method and the fitted spectra are shown in Fig. 2h. It shows the de-convoluted PL emission spectra of the sample with a prominent peak originating from $^6A_{1g} \rightarrow {}^4T_{1g}$ transition. In Fig. 2i we present the change of peak position ($^6A_{1g} \rightarrow {}^4T_{1g}$ transition) with interaction time. It is observed that with increasing interaction time, the peak position is red-shifted and after 120 min it is saturated. Thus, it clearly indicates the binding and adsorption of 34 nt long ssDNA on the 2D Mn_3O_4 nanosheets.

3.1. Development of a single-stranded DNA immobilized Mn_3O_4 nanomaterial-based biosensor surface for the detection of pathogen-associated RNA

To this end, we sought to design a 2D Mn_3O_4 decorated with an ssDNA surface that would be amenable to capture complementary nucleic acid sequences. For this purpose, an FAM (fluorescein)-labelled DNA oligonucleotide (Table 1) was mixed with 2D Mn_3O_4 to form a 2D metal oxide-DNA complex that was then immobilized on a UV sterilized glass slide for subsequent imaging using a fluorescence microscope (Leica Microsystems). FAM with an excitation peak at 493 nm and an emission peak at 517 nm will result in the observation of a green fluorescence signal for the FAM-labelled DNA. A glass slide coated with FAM-labelled DNA only solution was used as a negative control. As observed in Fig. 3a and c, in the absence of the 2D Mn_3O_4 metal oxide, only a minimal amount of the DNA was retained on the glass slide resulting in a low defused fluorescence signal throughout the field. Interestingly, complex formation with Mn_3O_4 helped the DNA to be retained on the glass surface in high quantity, resulting in bright fluorescence dots distributed throughout the field (Fig. 3b and d).

It could be inferred that the adsorption of DNA to Mn_3O_4 sheets leads to the local confinement of the DNA, thereby providing a concentrated green fluorescent signal of the FAM labelled DNA. This is a unique method of visually confirming

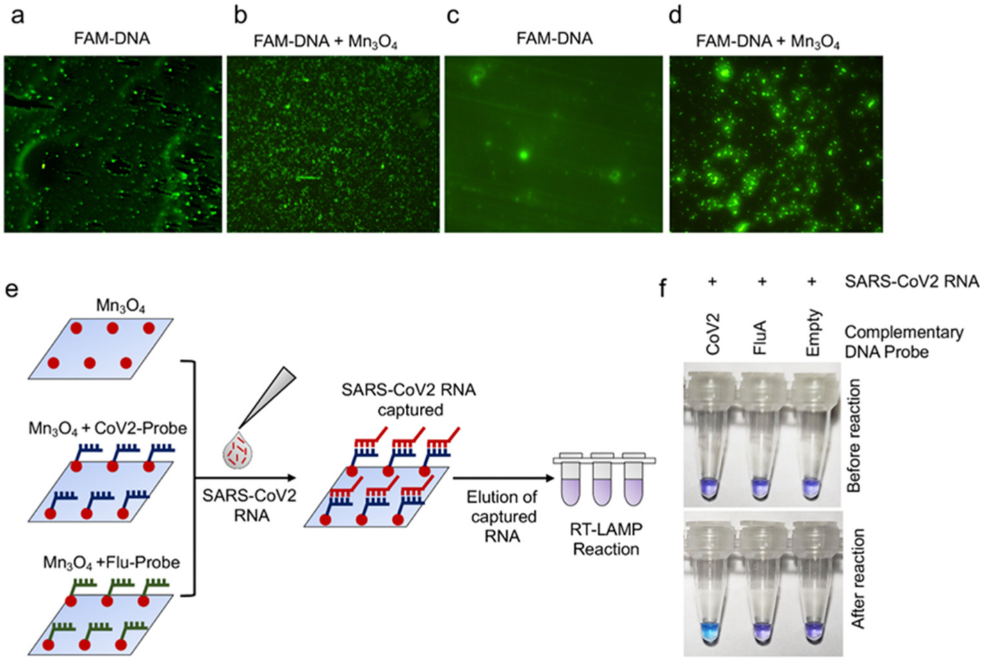

Fig. 3 ssDNA-immobilized Mn_3O_4 nanomaterial-based biosensor surface development. Visual detection of (a) FAM DNA, (b) FAM DNA+ 2D Mn_3O_4, (10× magnification), (c) FAM DNA, and (d) FAM DNA+ 2D Mn_3O_4 (45× magnification) as observed under a fluorescent microscope. (e) Schematic illustration of the systematic detection of complementary RNA by the SARS-CoV-2 RdRp specific ssDNA immobilized 2D Mn_3O_4 nanosheets. (f) Colorimetric LAMP reaction performed to show specific detection of the SARS-CoV-2 viral RNA by the complementary ssDNA adsorbed on 2D Mn_3O_4 nanosheets.

the adsorption of ssDNA on the Mn_3O_4 surface and paves a platform for the development of an ssDNA immobilized Mn_3O_4 surface-based biosensor chip for the capture and identification of the nucleic acids with complementary nucleotide sequences. Finally, we present an illustrative proposition for detecting viral nucleic acids using the ssDNA immobilized Mn_3O_4-based biosensing surface (Fig. 3e). For this purpose, we designed an experiment where the DNA-functionalized 2D nanomaterial surface was employed to capture contrived SARS-CoV-2 genomic RNA fragments. Single-stranded DNA oligonucleotides either complementary to the SARS-CoV-2 genome or to the influenza A virus genome were complexed with the Mn_3O_4 sheets before immobilizing them on the glass surface with the help of a PVDF coating agent. The functionalized surfaces where then subjected to incubation with an *in vitro* synthesized small RNA fragment (283 nucleotide) mimicking a specific region of the RNA-dependent RNA polymerase (RdRp) gene of SARS-CoV-2 followed by subsequent washing to remove the unbound RNA sample. Specific capturing of the SARS-CoV-2 RNA by the complementary DNA oligonucleotide was visualized by eluting the RNA from the surface and subsequently performing a colorimetric RT-LAMP reaction with specific sets of primers (Table S1, ESI†). As shown in Fig. 3f, surface-functionalized with complementary oligonucleotides resulted in specific retention of the SARS-CoV-2 RNA, hence giving a positive colorimetric readout in the RT-LAMP reaction (violet to blue). Surface-functionalization with either Mn_3O_4 alone or with non-specific oligonucleotides (complementary to the influenza A virus genome) resulted in no such colour change confirming the specificity of the biosensing surface. Together these experiments provide a proof of concept for the development of a novel single-stranded DNA-immobilized Mn_3O_4 as a biosensor for specific capturing of pathogen-associated nucleic acids.

3.2. Interaction mechanism: theoretical investigations on ssDNA-surface distance and number of contacts

A comprehensive theoretical analysis was carried out in order to clarify the mechanism behind the interaction between ss-DNA and 2D Mn_3O_4. Our simulations with single ssDNA and multiple ssDNA demonstrate that ssDNA gets adsorbed on the 2D Mn_3O_4 surface with the guanine bases at the 5′ end. Instantaneous snapshots of the system shown in Fig. 4a and b highlight this aspect.

To understand the nature of this interaction, we have computed the minimum distance between the 5′ end of ssDNA and Mn_3O_4, and the temporal evolution has been presented in Fig. 4c. It is noteworthy that the minimum distance is defined as the minimum of the all-atomic pair distances between the 5′guanine of ssDNA and Mn_3O_4 slab. From Fig. 4c, it can be easily seen that the minimum distance between 5′-guanine and the material surfaces initially decreased from 0.80 nm (0.27 ns) to an average value of ∼0.25 nm at ∼3.7 ns and remained steady at this average value for the rest of the simulation window. This indicates a steady adsorbed state of ssDNA on the Mn_3O_4 surface from 3.7 ns onward. Another essential aspect in the context of adsorption is the number of contacts formed between the adsorbate and adsorbent. In the present case, a contact is defined when one atom from ssDNA is within a distance of 0.4 nm from an atom of Mn_3O_4. The number of contacts was first found to be increasing from a starting value of ∼50 to ∼128 in 2.5 ns (Fig. 4d, inset). It then decreased to an average value of ∼70 around 7 ns (Fig. 4d, inset). Fluctuations in the number of contacts were observed at

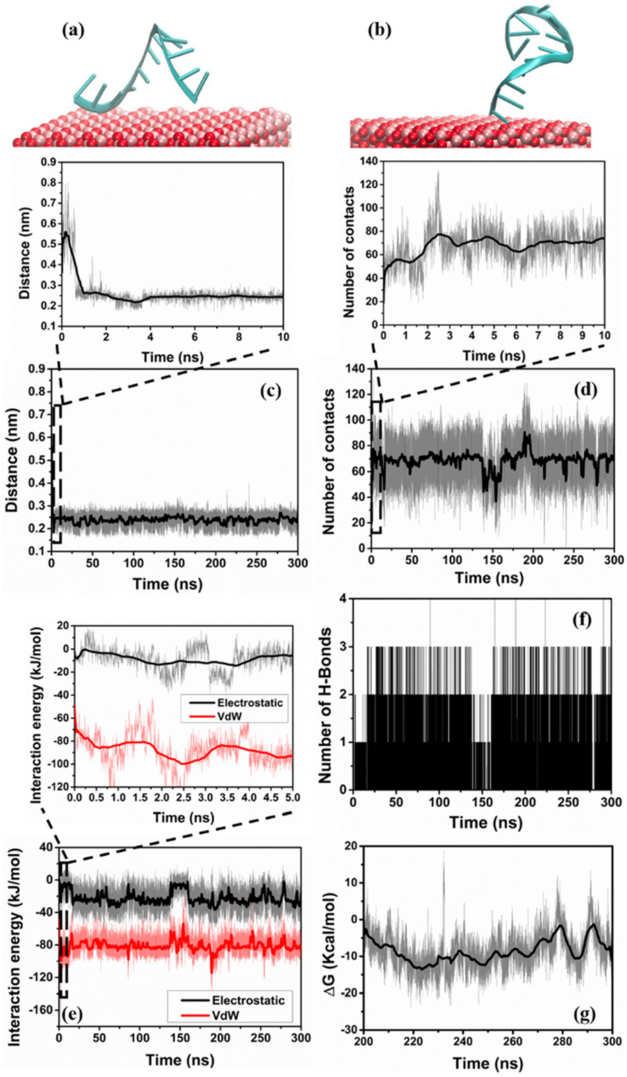

Fig. 4 Instantaneous snapshots of the system at (a) 0 ns and (b) 300 ns from the atomistic MD simulation. Water molecules have been removed for clarity. Surface is illustrated with VdW spheres with colour code: pink: Mn, red: O. ssDNA is presented using a "new Cartoon" representation scheme of VMD. (c) Temporal evolution of minimum distance between 5′-guanine and Mn_3O_4, (d) number of contacts, (e) interaction energy and (f) number of hydrogen bonds formed between ssDNA and material surfaces. (g) The variation of binding energy during the last 100 ns of simulation.

~150 ns and ~200 ns (Fig. 4d). The average number of contacts was recorded to be nearly constant at ~70 throughout the rest of the simulation time (Fig. 4d). In corroboration with the constant minimum distance, this also represents a steady adsorbed state. Note that the ssDNA undergoes conformational changes while having its 5′guanine mostly adsorbed on the surface. Earlier studies have shown that many small molecules exhibit several adsorbed conformations on flat attractive surfaces.[64]

3.3. *In silico* determination of ssDNA-Mn_3O_4 interaction and binding energy

The nature of the interaction between the ssDNA and the inorganic surface is of specific interest, as it is DNA-surface interaction, which drives the adsorption kinetics and stabilizes the DNA on the surface. The representative plots of the interaction energy between ssDNA and Mn_3O_4 clearly show that the adsorption is mainly dominated by the vdW interactions (Fig. 4e). The average vdW interaction energy was −81.58 ± 9.31 kJ mol^{-1}, whereas the average coulombic interaction energy was −20.86 ± 11.97 kJ mol^{-1}. In corroboration with the number of contacts data, the interaction energies also exhibited an initial increasing trend (absolute value), which is more prominent in the case of vdW interaction (Fig. 4e, inset). The average vdW interaction energy was increased from an initial value of ~−40 kJ mol^{-1} to ~−93 kJ mol^{-1} at ~5 ns (Fig. 4e, inset). On the other hand, the coulombic interaction rose from ~−2 kJ mol^{-1} (0 ns) to ~−5 kJ mol^{-1} at ~5 ns (Fig. 4e, inset). The significant contributions towards the interaction energy came from the 5′guanine (probably because of the different structure of 5′-guanine (no phosphate group) than the other guanines present in ssDNA), as shown in Fig. S2 in the ESI.† The 5′end of the ssDNA segment was adsorbed on the surface (Fig. 4b) and the rest of the DNA segment was free to move. 5′ guanine almost equally interacts with Mn and O atoms of the surface (Fig. S3 in the ESI†).

Another important mode of interaction that can tailor the adsorption kinetics is the formation of hydrogen bonds between DNA and the inorganic surface. The O atoms in the surface act as acceptors and the hydrogen atoms attached to the nitrogen atoms in the guanine base can act as donors. In the present study, the acceptor–donor cut-off distance to calculate the H-bonds was taken as 0.35 nm. The number of hydrogen bonds formed between the ssDNA and 2D Mn_3O_4 (001) surface has been depicted in Fig. 4f and it can be clearly seen that, although the adsorption kinetics is not regulated by hydrogen bond formation, it has a contribution towards the adsorption dynamics. Like before, the process of hydrogen bond formation also entirely took place between 5′ guanine and the surface (Fig. S4 in ESI†). In agreement with the number of contacts data, a decrease in the number of H-bonds formed between ssDNA and the 2D Mn_3O_4(001) surface can be seen ~150 ns (Fig. 4f).

In order to justify the spontaneity of the ssDNA adsorption on the Mn_3O_4(001) surface, the binding affinity/free energy of adsorption has been estimated using the MM-GBSA method, from the last 100 ns of the trajectory and the variation has been shown in Fig. 4g (neglecting the entropy contribution). The average binding energy was estimated to be −8.57 ± 5.03 kcal mol^{-1} (excluding entropy), which, consistent with the experimental findings, indicates the spontaneous binding of ssDNA segments on the Mn_3O_4 surface. On the other hand, the change in the rotational ($T\Delta S_{\mathrm{rot}}$) and translational entropy ($T\Delta S_{\mathrm{trans}}$) values was found to be −2.46 kcal mol^{-1} and −16.05 kcal mol^{-1}, respectively. The negative entropy change indicates the loss of rotational and translational degrees of freedom of ssDNA upon binding with the Mn_3O_4 surface.

3.4. Surface-dependent structural changes of ssDNA: computational observations

The structural change during the adsorption process is a crucial aspect to study as the structural change upon adsorption can affect the functionality of the adsorbed molecules. In the present study, the root mean square deviation (RMSD) and radius of gyration of the ssDNA segment have been calculated to get an insight into the effects of the presence of the Mn_3O_4 on the structure of the ssDNA.

To understand the structural fluctuation of ssDNA in the presence of the substrate, we have calculated the RMSD of the ssDNA as a function of time both in the presence and absence of the substrate. The time evolution of the RMSD is shown in Fig. 5a. The ssDNA segment underwent significant structural deviations, irrespective of the presence of the inorganic surface (Fig. 5a). The adsorbed ssDNA remained mostly stable from 40 ns onward (Fig. 5a), whereas the fluctuation in RMSD was more prominent in the absence of the surface. This observation implies that the adsorption of ssDNA on the material slabs imposes a structural stabilization on the former. The stability of ssDNA on the 2D Mn_3O_4 surface is also consistent with the negative change in translational and rotational entropy values stated in the previous section.

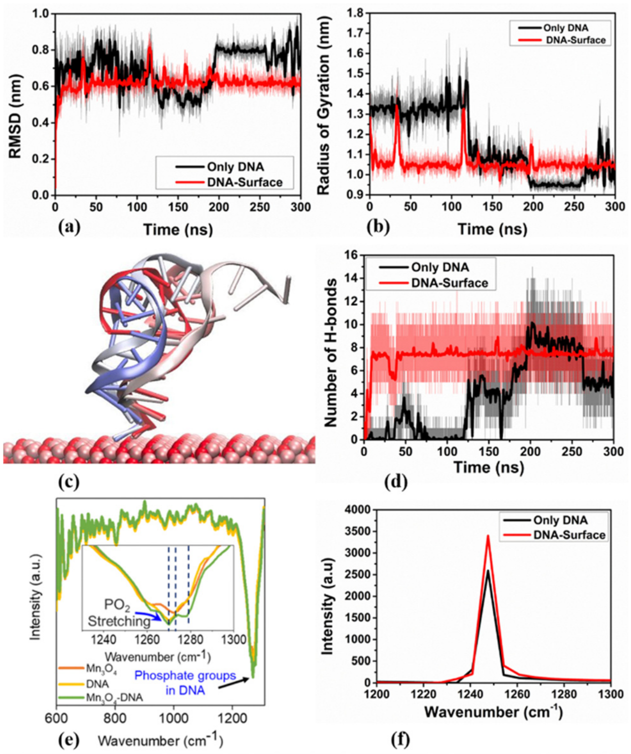

Fig. 5 The presence of a surface significantly affects the ssDNA structure. Variation of (a) RMSD, and (b) radius of gyration during the course of simulation. (c) A snapshot of the system showing unfolding and folding of ssDNA between 30 and 38 ns. Water molecules have been removed for clarity. The surface is illustrated with VdW spheres with colour code: pink: Mn, red: O. ssDNA is presented using a "new Cartoon" representation scheme of VMD with colour code: red: folded ssDNA at 30 ns; white: intermediate unfolded ssDNA; and blue: folded ssDNA at 38 ns. (d) Temporal variation of intramolecular H-bonds in the presence and absence of surface. (e) Experimental FTIR spectrum of DNA and (f) computed power spectrum of the phosphate groups of ssDNA. (e) Inset illustrates the experimentally observed changes of FTIR spectrum of phosphate group of DNA in presence of Mn_3O_4.

To get a better comprehension of the size and compactness of the ssDNA segment, the radius of gyration (R_g) of the adsorbed ssDNA was calculated and compared to R_g of the same ssDNA segment in the absence of surface (Fig. 5b). It is evident from the figure that the presence of an inorganic slab caused the ssDNA segment to become more compact for the first 150 ns and the compactness was achieved within the first 7 ns of the simulation (Fig. 5b). The ssDNA strand only in water became more compact between 200 and 250 ns, but again began to unfold (Fig. 5b). Together with the RMSD data, the trend of the radius of gyration also indicates that the adsorption phenomena stabilize the ssDNA structure on the surface. One striking feature is the sudden rise and fall of R_g between 30 ns and 40 ns, and again between 110 and 120 ns (Fig. 5b). The RMSD also exhibited similar behavior in these time windows (Fig. 5a). In the time window between 30 and 40 ns, the ssDNA unfolded itself to some extent and then folded back again (Fig. 5c), which caused the jump in R_g, and RMSD. Similar unfolding and folding of ssDNA took place between 110 and 120 ns, as well (figure not shown). It is well known that the DNA structure stabilizes through intra-molecular hydrogen formation. Therefore, the number of intra-molecular hydrogen bonds was calculated and is presented in Fig. 5d. Because of its compact structure, the adsorbed ssDNA formed significantly more intramolecular hydrogen bonds; except between 200 ns and 250 ns, when the ssDNA in the absence of the surface became more compact (Fig. 5d).

In harmony with the previous arguments, the higher number of intramolecular H-bonds in the adsorbed ssDNA (for most of the simulation window) is another piece of evidence of the greater structural stability. Another notable observation is that the number of H-bonds in ssDNA simulated in the water only showed a slight increment between 40 and 60 ns (Fig. 5d). The DNA became slightly folded in this time window, as seen from the lower R_g values (Fig. 5b), which resulted in the formation of more intramolecular H-bonds. With an aim to acquire a better understanding of the experimentally obtained FTIR spectra, the power spectrum of the phosphate groups has been calculated by taking the Fourier transform of the velocity autocorrelation function of the phosphate groups. The computed spectrum as shown in Fig. 5f is in the range from 1200 cm^{-1} to 1300 cm^{-1}. The calculated peak position ($\sim$1250 cm^{-1}) was quite close to the experimental observation (1275 cm^{-1}) (Fig. 5e). Moreover, in agreement with the experimental results, the intensity of the $PO_4{}^{3-}$ vibrational peaks changed in the presence of the surface. This can be attributed to the more stable structure of the adsorbed ssDNA (Fig. 5b). It is well known that, the spectral intensity and vibrational frequency of a particular functional group changes in the presence of hydrogen bonds.[59,65] Because the structure of ssDNA remained stable in the presence of the surface, the adsorbed ssDNA formed more intramolecular hydrogen bonds on average (7.29 ± 1.35) than its counterpart in water only (3.75 ± 3.39), which affected the spectral density.

4. Conclusions

In the present study, we have successfully demonstrated the interaction of ssDNA with 2D Mn_3O_4. The interaction dynamics of the ss-DNA with 2D Mn_3O_4 have been analyzed through optical absorption, photoluminescence spectroscopy and fluorescent microscopy. We also envision single-stranded DNA-immobilized 2D Mn_3O_4 as a biosensor for specific capturing of pathogen-associated nucleic acids. We hereby present the proof of concept for a novel, rapid and cost-effective portable 2D Mn_3O_4-based biosensor that can specifically detect SARS CoV2 and a wide variety of other pathogen-associated nucleic acids from a patient's samples. The 2D Mn_3O_4 surface functionalized with complementary ssDNA oligonucleotide resulted in specific retention of the SARS-CoV-2 RNA by the principle of DNA–RNA hybridization thereby giving a positive colorimetric readout in the RT-LAMP reaction with high specificity. The computational techniques have been successfully employed to infer the experimentally observed ssDNA-Mn_3O_4 interaction in atomic detail. VdW interaction is observed to be the driving force behind the adsorption phenomenon, with 5′-guanine the most interacting nucleotide. The adsorption of ssDNA on the inorganic surface was also driven by favourable (negative) enthalpy change. Moreover, the presence of the surface also caused the ssDNA to stabilize, which led to a higher average number of intramolecular H-bond formations, resulting in a change in the spectral density, consistent with the experimental observations. Therefore, we believe that our understanding of this interface (DNA-2D Mn_3O_4) may be helpful in facilitating the development of a biosensor that might serve as an avenue platform for the detection of a wide range of pathogen-related nucleic acids in a clinical scenario.

Conflicts of interest

The authors declare no conflicts of interest.

Acknowledgements

P. K. and C. S. T. acknowledge Indian Institute of Technology Kharagpur for laboratory facility. C. S. T. also acknowledges Ramanujan fellowship and core research grant of SERB, India and the funding received from STARS project by MHRD, India and ISRO, India.

References

1 G. Seo, G. Lee, M. J. Kim, S.-H. Baek, M. Choi, K. B. Ku, C.-S. Lee, S. Jun, D. Park and H. G. Kim, Rapid detection of COVID-19 causative virus (SARS-CoV-2) in human nasopharyngeal swab specimens using field-effect transistor-based biosensor, *ACS Nano*, 2020, **14**, 5135–5142.

2 S. Mahari, A. Roberts, D. Shahdeo and S. Gandhi, *eCovSens-ultrasensitive novel in-house built printed circuit board based electrochemical device for rapid detection of nCovid-19*, BioRxiv, 2020, 2004–2020.

3 A. Djaileb, B. Charron, M. H. Jodaylami, V. Thibault, J. Coutu, K. Stevenson, S. Forest, L. S. Live, D. Boudreau and J. N. Pelletier, A rapid and quantitative serum test for SARS-CoV-2 antibodies with portable surface plasmon resonance sensing, *ChemRxiv*, 2020, preprint, DOI: **10.26434/chemrxiv.12118914.v1**.

4 A. Chakravarthy, A. Nandakumar, G. George, S. Ranganathan, S. Umashankar, N. Shettigar, D. Palakodeti, A. Gulyani and A. Ramesh, Engineered RNA biosensors enable ultrasensitive SARS-CoV-2 detection in a simple color and luminescence assay, *Life Sci. Alliance*, 2021, **4**, e202101213.

5 P. Moitra, M. Alafeef, M. Alafeef, M. Alafeef, K. Dighe, M. B. Frieman, D. Pan, D. Pan and D. Pan, Selective Naked-Eye Detection of SARS-CoV-2 Mediated by N Gene Targeted Antisense Oligonucleotide Capped Plasmonic Nanoparticles, *ACS Nano*, 2020, **14**, 7617–7627.

6 H. Kim, M. Park, J. Hwang, J. H. Kim, D. R. Chung, K. Lee and M. Kang, Development of Label-Free Colorimetric Assay for MERS-CoV Using Gold Nanoparticles, *ACS Sens.*, 2019, **4**, 1306–1312.

7 S. E. Ochmann, C. Vietz, K. Trofymchuk, G. P. Acuna, B. Lalkens and P. Tinnefeld, Optical Nanoantenna for Single Molecule-Based Detection of Zika Virus Nucleic Acids without Molecular Multiplication, *Anal. Chem.*, 2017, **89**, 13000–13007.

8 S. Banerjee, S. K. Biswas, N. Kedia, R. Sarkar, A. De, S. Mitra, S. Roy, R. Chowdhury, S. Samaddar and A. Bandopadhyay, Piecewise isothermal nucleic acid testing (PINAT) for infectious disease detection with sample-to-result integration at the point-of-care, *ACS Sens.*, 2021, **6**, 3753–3764.

9 R. Singh, M. Das Mukherjee, G. Sumana, R. K. Gupta, S. Sood and B. D. Malhotra, Biosensors for pathogen detection: A smart approach towards clinical diagnosis, *Sens. Actuators, B*, 2014, **197**, 385–404.

10 C. Roh, A facile inhibitor screening of hepatitis C virus NS3 protein using nanoparticle-based RNA, *Biosensors*, 2012, **2**, 427–432.

11 C. H. Lin, C. H. Hung, C. Y. Hsiao, H. C. Lin, F. H. Ko and Y. S. Yang, Poly-silicon nanowire field-effect transistor for ultrasensitive and label-free detection of pathogenic avian influenza DNA, *Biosens. Bioelectron.*, 2009, **24**, 3019–3024.

12 L. T. H. Kao, L. Shankar, T. G. Kang, G. Zhang, G. K. I. Tay, S. R. M. Rafei and C. W. H. Lee, Multiplexed detection and differentiation of the DNA strains for influenza A (H1N1 2009) using a silicon-based microfluidic system, *Biosens. Bioelectron.*, 2011, **26**, 2006–2011.

13 G. J. Zhang, L. Zhang, M. J. Huang, Z. H. H. Luo, G. K. I. Tay, E. J. A. Lim, T. G. Kang and Y. Chen, Silicon nanowire biosensor for highly sensitive and rapid detection of Dengue virus, *Sens. Actuators, B*, 2010, **146**, 138–144.

14 T. S. Bronder, A. Poghossian, S. Scheja, C. Wu, M. Keusgen, D. Mewes and M. J. Schöning, DNA immobilization and hybridization detection by the intrinsic molecular charge using capacitive field-effect sensors modified with a charged weak polyelectrolyte layer, *ACS Appl. Mater. Interfaces*, 2015, **7**, 20068–20075.

15 A. G. Cherstvy, Detection of DNA hybridization by field-effect DNA-based biosensors: mechanisms of signal generation and open questions, *Biosens. Bioelectron.*, 2013, **46**, 162–170.

16 G. Qiu, Z. Gai, Y. Tao, J. Schmitt, G. A. Kullak-Ublick and J. Wang, Dual-functional plasmonic photothermal biosensors

for highly accurate severe acute respiratory syndrome coronavirus 2 detection, *ACS Nano*, 2020, **14**, 5268–5277.

17 C. L. Manzanares-Palenzuela, A. M. Pourrahimi, J. Gonzalez-Julian, Z. Sofer, M. Pykal, M. Otyepka and M. Pumera, Interaction of single- and double-stranded DNA with multilayer MXene by fluorescence spectroscopy and molecular dynamics simulations, *Chem. Sci.*, 2019, **10**, 10010–10017.

18 B. Luan and R. Zhou, Spontaneous ssDNA stretching on graphene and hexagonal boron nitride in plane heterostructures, *Nat. Commun.*, 2019, **10**, 1–6.

19 Z. Huang, B. Liu and J. Liu, Mn2 + -assisted DNA oligonucleotide adsorption on Ti2C MXene nanosheets, *Langmuir*, 2019, **35**, 9858–9866.

20 B. Ren and Y. Wang, Engineering two-dimensional metal oxides via surface functionalization for biological applications, *J. Mater. Chem. B*, 2020, **8**, 1108–1127.

21 I. Gessner, J. W. U. Fries, V. Brune and S. Mathur, Magnetic nanoparticle-based amplification of microRNA detection in body fluids for early disease diagnosis, *J. Mater. Chem. B*, 2021, **9**, 9–22.

22 Z. Liu, L. Ma, G. Shi, W. Zhou, Y. Gong, S. Lei, X. Yang, J. Zhang, J. Yu, K. P. Hackenberg, A. Babakhani, J. C. Idrobo, R. Vajtai, J. Lou and P. M. Ajayan, In-plane heterostructures of graphene and hexagonal boron nitride with controlled domain sizes, *Nat. Nanotechnol.*, 2013, **8**, 119–124.

23 C. Huang, S. Wu, A. M. Sanchez, J. J. P. Peters, R. Beanland, J. S. Ross, P. Rivera, W. Yao, D. H. Cobden and X. Xu, Lateral heterojunctions within monolayer MoSe2-WSe2 semiconductors, *Nat. Mater.*, 2014, **13**, 1096–1101.

24 Y. Gong, J. Lin, X. Wang, G. Shi, S. Lei, Z. Lin, X. Zou, G. Ye, R. Vajtai, B. I. Yakobson, H. Terrones, M. Terrones, B. K. Tay, J. Lou, S. T. Pantelides, Z. Liu, W. Zhou and P. M. Ajayan, Vertical and in-plane heterostructures from WS 2/MoS 2 monolayers, *Nat. Mater.*, 2014, **13**, 1135–1142.

25 X. Duan, C. Wang, J. C. Shaw, R. Cheng, Y. Chen, H. Li, X. Wu, Y. Tang, Q. Zhang, A. Pan, J. Jiang, R. Yu, Y. Huang and X. Duan, Lateral epitaxial growth of two-dimensional layered semiconductor heterojunctions, *Nat. Nanotechnol.*, 2014, **9**, 1024–1030.

26 A. K. Geim, Graphene: Status and prospects, *Science*, 2009, **324**, 1530.

27 A. Ambrosi, C. K. Chua, A. Bonanni and M. Pumera, Electrochemistry of graphene and related materials, *Chem. Rev.*, 2014, **114**, 7150–7188.

28 L. Zhao, J. Wang, D. Su, Y. Zhang, H. Lu, X. Yan, J. Bai, Y. Gao and G. Lu, The DNA controllable peroxidase mimetic activity of MoS2nanosheets for constructing a robust colorimetric biosensor, *Nanoscale*, 2020, **12**, 19420–19428.

29 N. Asefifeyzabadi, R. Alkhaldi, A. Z. Qamar, A. A. Pater, M. Patwardhan, K. T. Gagnon, S. Talapatra and M. H. Shamsi, Label-free Electrochemical Detection of CGG Repeats on Inkjet Printable 2D Layers of MoS2, *ACS Appl. Mater. Interfaces*, 2020, **12**, 52156–52165.

30 C. Lu, Y. Liu, Y. Ying and J. Liu, Comparison of MoS2, WS2, and graphene oxide for DNA adsorption and sensing, *Langmuir*, 2017, **33**, 630–637.

31 C. Zhu, Z. Zeng, H. Li, F. Li, C. Fan and H. Zhang, Single-layer MoS2-based nanoprobes for homogeneous detection of biomolecules, *J. Am. Chem. Soc.*, 2013, **135**, 5998–6001.

32 S. Wang, S. Wei, S. Wang, X. Zhu, C. Lei, Y. Huang, Z. Nie and S. Yao, Chimeric DNA-Functionalized Titanium Carbide MXenes for Simultaneous Mapping of Dual Cancer Biomarkers in Living Cells, *Anal. Chem.*, 2019, **91**, 1651–1658.

33 J. C. Wu, X. Peng, Y. Q. Guo, H. D. Zhou, J. Y. Zhao, K. Q. Ruan, W. S. Chu and C. Wu, Ultrathin nanosheets of Mn3O4: A new two-dimensional ferromagnetic material with strong magnetocrystalline anisotropy, *Front. Phys.*, 2018, **13**, 138110.

34 X. Hao, J. Zhao, Y. Li, Y. Zhao, D. Ma and L. Li, Mild aqueous synthesis of octahedral Mn3O4 nanocrystals with varied oxidation states, *Colloids Surf., A*, 2011, **374**, 42–47.

35 T. M. Project, 2020.

36 R. Picciochi, J. N. Canongia Lopes, H. P. Diogo and M. E. Minas da Piedade, Experimental and Molecular Dynamics Simulation Study of the Sublimation Energetics of Cyclopentadienyltricarbonylmanganese (Cymantrene), *J. Phys. Chem. A*, 2008, **112**, 10429–10434.

37 J. N. Canongia Lopes, P. Cabral do Couto and M. E. Minas da Piedade, An All-Atom Force Field for Metallocenes, *J. Phys. Chem. A*, 2006, **110**, 13850–13856.

38 M. Frisch and F. Clemente, M. J. Frisch, G. W. Trucks, H. B. Schlegel, G. E. Scuseria, M. A. Robb, J. R. Cheeseman, G. Scalmani, V. Barone, B. Mennucci, G. A. Petersson, H. Nakatsuji, M. Caricato, X. Li, H. P. Hratchian, A. F. Izmaylov, J. Bloino and G. Zhe, *Gaussian 09, Revision A.01*, 2016.

39 J. Wang, W. Wang, P. A. Kollman and D. A. Case, Automatic atom type and bond type perception in molecular mechanical calculations, *J. Mol. Graph. Model.*, 2006, **25**, 247–260.

40 T. J. Macke and D. A. Case, *ACS Symp. Ser.*, 1998, **682**, 379–393.

41 M. Zgarbová, J. Sponer, M. Otyepka, T. E. Cheatham III, R. Galindo-Murillo and P. Jurecka, Refinement of the sugar–phosphate backbone torsion beta for AMBER force fields improves the description of Z-and B-DNA, *J. Chem. Theory Comput.*, 2015, **11**, 5723–5736.

42 G. Bussi, D. Donadio and M. Parrinello, Canonical sampling through velocity rescaling, *J. Chem. Phys.*, 2007, **126**, 14101.

43 H. J. C. Berendsen, J. P. M. van Postma, W. F. van Gunsteren, A. DiNola and J. R. Haak, Molecular dynamics with coupling to an external bath, *J. Chem. Phys.*, 1984, **81**, 3684–3690.

44 M. Parrinello and A. Rahman, Polymorphic transitions in single crystals: A new molecular dynamics method, *J. Appl. Phys.*, 1981, **52**, 7182–7190.

45 B. Hess, H. Bekker, H. J. C. Berendsen and J. G. E. M. Fraaije, LINCS: a linear constraint solver for molecular simulations, *J. Comput. Chem.*, 1997, **18**, 1463–1472.

46 T. Darden, D. York and L. Pedersen, Particle mesh Ewald: An N·log (N) method for Ewald sums in large systems, *J. Chem. Phys.*, 1993, **98**, 10089–10092.

47 M. J. Abraham, T. Murtola, R. Schulz, S. Páll, J. C. Smith, B. Hess and E. Lindah, Gromacs: High performance

molecular simulations through multi-level parallelism from laptops to supercomputers, *SoftwareX*, 2015, **1–2**, 19–25.

48 W. Humphrey, A. Dalke and K. Schulten, VMD: visual molecular dynamics, *J. Mol. Graph.*, 1996, **14**, 33–38.

49 M. Ylilauri and O. T. Pentikäinen, MMGBSA as a tool to understand the binding affinities of filamin–peptide interactions, *J. Chem. Inf. Model.*, 2013, **53**, 2626–2633.

50 M. S. Valdés-Tresanco, M. E. Valdés-Tresanco, P. A. Valiente and E. Moreno, gmx_MMPBSA: A New Tool to Perform End-State Free Energy Calculations with GROMACS, *J. Chem. Theory Comput.*, 2021, **17**, 6281–6291.

51 B. R. Miller, T. D. Mcgee, J. M. Swails, N. Homeyer, H. Gohlke and A. E. Roitberg, MMPBSA. py: An Efficient Program for End-State Free Energy Calculations, *J. Chem. Theory Comput.*, 2012, **8**, 3314–3321.

52 S.-T. Lin, M. Blanco and W. A. Goddard III, The two-phase model for calculating thermodynamic properties of liquids from molecular dynamics: Validation for the phase diagram of Lennard-Jones fluids, *J. Chem. Phys.*, 2003, **119**, 11792–11805.

53 S.-T. Lin, P. K. Maiti and W. A. Goddard III, Two-phase thermodynamic model for efficient and accurate absolute entropy of water from molecular dynamics simulations, *J. Phys. Chem. B*, 2010, **114**, 8191–8198.

54 P. K. Maiti and B. Bagchi, Structure and dynamics of DNA–dendrimer complexation: role of counterions, water, and base pair sequence, *Nano Lett.*, 2006, **6**, 2478–2485.

55 B. Nandy and P. K. Maiti, DNA compaction by a dendrimer, *J. Phys. Chem. B*, 2011, **115**, 217–230.

56 V. Vasumathi and P. K. Maiti, Complexation of siRNA with dendrimer: a molecular modeling approach, *Macromolecules*, 2010, **43**, 8264–8274.

57 M. Santosh, S. Panigrahi, D. Bhattacharyya, A. K. Sood and P. K. Maiti, Unzipping and binding of small interfering RNA with single walled carbon nanotube: a platform for small interfering RNA delivery, *J. Chem. Phys.*, 2012, **136**, 02B611.

58 V. C. Bose and V. Biju, Optical, electrical and magnetic properties of nanostructured Mn3O4 synthesized through a facile chemical route, *Phys. E*, 2015, **66**, 24–32.

59 T. Fornaro, D. Burini, M. Biczysko and V. Barone, Hydrogen-bonding effects on infrared spectra from anharmonic computations: uracil–water complexes and uracil dimers, *J. Phys. Chem. A*, 2015, **119**, 4224–4236.

60 M. P. Kushalkar, B. Liu and J. Liu, Promoting DNA adsorption by acids and polyvalent cations: Beyond charge screening, *Langmuir*, 2020, **36**, 11183–11195.

61 Z. Huang, Y. Zhao, B. Liu, S. Guan and J. Liu, Stronger Adsorption of Phosphorothioate DNA Oligonucleotides on Graphene Oxide by van der Waals Forces, *Langmuir*, 2020, **36**, 13708–13715.

62 I. Roy, Q. Wang and V. Chakrapani, Nature of Reaction Intermediates and Origin of Bifunctionality in Manganese Oxide, *J. Phys. Chem. C*, 2020, **124**, 5286–5299.

63 R. Mićić and B. Drašković, Some Photoluminescence Properties of Mn2+ in Magnesium Bromide, *Phys. Status Solidi*, 1985, **128**, 489–494.

64 A. D. Fernández, P. Charchar, A. G. Cherstvy, R. Metzler and M. W. Finnis, The diffusion of doxorubicin drug molecules in silica nanoslits is non-Gaussian, intermittent and anticorrelated, *Phys. Chem. Chem. Phys.*, 2020, **22**, 27955–27965.

65 B. Athokpam, S. G. Ramesh and R. H. McKenzie, Effect of hydrogen bonding on the infrared absorption intensity of OH stretch vibrations, *Chem. Phys.*, 2017, **488**, 43–54.